

Péclet dependent Interactions of Self-Propelled Droplets

Prateek Dwivedi, Sobiya Ashraf, Pawan Kumar, Dipin Pillai, and Rahul Mangal*
Department of Chemical Engineering, Indian Institute of Technology Kanpur, Kanpur, India.

Interactions among biologically active agents is facilitated by their self-generated chemical and hydrodynamic fields. In order to elucidate the pair-wise interactions between such micro-organisms, we employ active droplets as a model system, capable of self-generating chemical and hydrodynamic fields. We demonstrate that the solute Péclet number (Pe), characterizing the relative strength of its convective to diffusive transport, plays a crucial role in determining how the chemical and hydrodynamic fields impact their interactions. Our findings reveal that at low Pe , the interaction is predominantly governed by chemo-repulsive effects, leading to droplets avoiding physical contact. Conversely, at elevated Pe , hydrodynamic interactions become more influential, leading to physical engagement. However, irrespective of Pe , the interaction of a droplet with the chemical trail of another droplet is always governed by chemo-repulsive effects. Furthermore, our results establish that the chemo-repulsive deflection/rebounding of droplets is influenced by the droplets' inherent chemical polarity, as determined by its Pe , independent of their approach orientation. Our findings offer a methodology for tuning the outcomes of binary interactions among chemically active droplets, laying the groundwork for potential studies on their collective dynamics.

I. INTRODUCTION

Artificial micro-swimmers use anisotropic interactions with their surroundings to achieve out-of-equilibrium self-propulsion. One such popular route to self-propulsion is the use of Janus particles (JPs), which possess an intrinsic asymmetry in their physical/chemical morphology. Under suitable conditions, this asymmetry facilitates a physico-chemical gradient in their surrounding, propelling them through a mechanism known as “phoresis” [1]. Depending on the exact mechanism behind the gradient generation, JPs may self-propel via self-diffusiophoresis [2, 3], self-thermophoresis [4, 5] or self-electrophoresis [6, 7]. In case of active droplets, the absence of any inherent geometric/compositional asymmetry necessitates an alternate chemical pathway to spontaneously generate asymmetry in the interfacial tension (γ) gradient along the droplet interface. The resulting Marangoni stress drives the fluid flow from regions of low to high interfacial tension, resulting in droplet propulsion in the opposite direction. Among the different mechanisms known to generate interfacial tension gradient, micellar solubilization based mechanism is very popular [8–11]. When oil (water) droplets are dispersed in an aqueous (oil) continuous phase containing surfactant at high concentration, typically \gg critical micellar concentration (CMC), the droplets undergo solubilization releasing myriad of filled micelles. This solubilization is facilitated by the loss of some surfactants absorbed at the interface, which spontaneously generates the desired gradient of interfacial surfactant coverage. Once the droplet motion is initiated, the advective transport of fresh surfactant/empty micelles, which couples non-linearly with the droplet motion, leads to sustained self-propulsion [12].

Using an axi-symmetric 2D model of a self-propelled

active droplet accounting for diffusiophoretic and Marangoni effects, Morozov and Michellin demonstrated that a dimensionless Pe number governs the mode of swimming [12]. Beyond a critical Pe i.e. 4, sustained self-propulsion is predicted. A further increase in Pe leads to chaotic motion due to the emergence of higher order modes, hindering the front-aft asymmetry. For swimming oil droplets in aqueous media, recent experiments have verified this prediction either by increasing the surfactant concentration [13], by adding molecular solutes [14, 15] or by changing the droplet size [16, 17]. Recently, using macro-molecular additives, Dwivedi *et al.* demonstrated that a significantly low Pe can be attained, resulting in persistent motion, a regime which until recent past was inaccessible in simple Newtonian aqueous media [18]. The persistent motion was attributed to the emergence of the puller swimming mode at lower Pe , in which the droplet pulls the fluid from its leading and trailing edge and pushes out from its sides. Very recently, for 5CB droplets in aqueous solution containing sodium dodecyl sulphate (SDS) as surfactant, Kumar *et al.* tuned the concentration of filled micelles as a means to attain lower Pe , resulting in puller mode [19]. In another recent study, Dwivedi *et al.* further demonstrated experimentally that upon rendering the continuous media viscoelastic, the droplets deform from their usual spherical shape. Using a simple analytical model they elucidated that the shape deformation was due to the excess normal stress at the droplet interface generated by the deformed polymer chains [20].

These active droplets have been shown to exhibit intriguing phenomena commonly observed in microbial motion, such as chemotaxis [21], rheotaxis [22, 23], and motion under gravity [24]. Apart from the fascinating characteristics displayed by isolated swimming droplets, their collective behavior has also garnered significant interest. The study of collective dynamics in these droplets

* mangalr@iitk.ac.in

offers valuable insights into the collective behavior observed in biological microswimmers, including flocking or swarming [25], predator-prey interactions [26], the formation of bacterial colonies [27], and inter-cellular communications. Furthermore, the collective behavior of these artificial swimmers enables them to accomplish tasks that would otherwise be unattainable by isolated swimmers. For instance, recent studies have reported formation of dynamic self-assemblies that can evolve into new structures depending on upon the physical confinement or nature of activity [28]. Spontaneous rotation of such dynamic clusters has also been reported [29]. A few recent studies explored chemotactic interaction between an oil droplet in an aqueous surfactant solution and chemical trail of another droplet [30], and by varying the chemical structure and concentration of oils and surfactants, thereby mimicking predator-prey dynamics [31].

The emergence of collective dynamics in these systems is a result of the pairwise interactions between the swimmers. In biological swimmers the interactions are mostly governed by chemical signalling and hydrodynamics mediated by the intermediate fluid. The hydrodynamic signature of a swimmer depends on its size, speed, physical confinement and more importantly on its swimming mode. For example, pushers are known to push the fluid from their front and rear end and pull from their equatorial region, whereas, pullers do the opposite [32]. In active droplets, besides the short ranged hydrodynamic interactions, the chemical field generated by the swimmers play a vital role in their interactions. For micellar solubilization based active droplets, the trail of filled micelles released by the swimming droplets is generally avoided by other droplets. The transport of free surfactants toward regions rich in filled micelles is hindered by electrostatic repulsion, and therefore such regions serve as fuel depleted domain for the other droplets which they intentionally avoid, a phenomenon known as negative chemotaxis [21]. These chemical interactions are expected to depend various factors such as rate of droplet rate of solubilization, medium viscosity, droplet size etc. These factors are captured by the advection-diffusion model via i.e. Pe associated with droplet motion.

Despite recent progress, pair interactions and the resultant collective dynamics have been limited to swimming droplets with a pusher mode of propulsion. These investigations were also limited to moderate Pe , with weak chemical signature allowing hydrodynamic interactions to dominate. Recently, in 2021, Lippera *et al.* theoretically predicted repulsive pair-collisions between droplets when interacting through chemical fields only at low Pe [33]. No other study has explored pair interactions of such swimmers in detail. Therefore, to gain a comprehensive understanding, in this work, we experimentally explore the pair interactions of swimming droplets over a wide range of droplet Pe . High Pe droplets are generated

in usual aqueous media wherein droplets propel as pushers. Lower Pe propulsion was achieved by adding macromolecules to the surrounding medium, wherein, droplets propel as pullers. The study reveals strong repulsive interaction among the droplets with lower Pe , leading to strongly scattering collisions. On the other hand, for higher Pe , the presence of stronger hydrodynamic interactions can lead to a variety of two-body interactions.

II. MATERIALS AND METHODS

Using DI water, an aqueous solution containing 6 wt.% Trimethyl ammonium bromide (TTAB), a cationic surfactant obtained from Loba Chemicals, was prepared. In some experiments, 1 wt.% Polyethylene oxide (PEO) with a molecular weight of 8000 kDa, sourced from Sigma Aldrich, was added to the aqueous TTAB solution as a macromolecular solute. Droplets ($\sim 50 \mu\text{m}$) of 4-Cyano-4'-pentylbiphenyl (5CB), a thermotropic liquid crystal acting as the oil phase, also procured from Sigma Aldrich, were formed using a micro-injector (Femtojet 4i, Eppendorf) by injecting 5CB into the TTAB solution (with or without polymer solute). The resulting emulsion was then injected into a custom-built Hele-Shaw optical cell with a vertical gap of $100 \mu\text{m}$. The cell was prepared using glass slides cleaned through ultrasonication in ethanol, followed by plasma treatment and nitrogen drying. Considering gap thickness to be marginally larger than the droplet size, this setup restricted droplet movement mostly to a 2D X-Y plane (fig. 1(a)). Droplet trajectories ($X(t), Y(t)$) were captured using Image-J software equipped with Mtrack2 plugin. The time-averaged speed of the droplets was computed as $V = \left\langle \left| \frac{\mathbf{r}_{i+1} - \mathbf{r}_i}{t_{i+1} - t_i} \right| \right\rangle$, where $\mathbf{r}_i = \{X_i(t), Y_i(t)\}$, is the position vector of the droplet center at the i^{th} time instant.

The chemical field around the droplets was optically visualized by incorporating Nile Red, an oil-soluble fluorescent dye, obtained from Sigma Aldrich, into the 5CB oil droplets. To analyze the fluid flow around the droplets, Particle Image Velocimetry (PIV) was employed. In this technique, fluorescent polystyrene particles ($\sim 500 \text{ nm}$) procured from Thermo Scientific were dispersed in the surfactant solution, which are convected by the flow-field generated by the swimming droplets. The optical setup includes mounting the Hele-Shaw cell on an Olympus IX73 inverted microscope, equipped with an Olympus U-RFL-T fluorescence illuminator (Mercury Burner USH-1030L) and a laser (wavelength approximately 560 nm) for dye excitation. A FLIR ORX-10G-71S7C-C camera (3208 x 2200 pixels), attached to the microscope with 10x magnification, and controlled via a computer interface (SpinView software), captured videos with consistent exposure settings. The velocity vectors around the droplets were computed using the PIVlab open-source software in

MATLAB, as cited in [34].

III. RESULTS AND DISCUSSION

A. Micellar solubilization and swimming mode

Due to the TTAB concentration (=6 wt.%) being significantly above its CMC (=0.13 wt.%), 5CB droplets undergo micellar solubilization-based self-propulsion in aqueous TTAB solution (cf. fig. 1(b) for a schematic of propulsion). The droplets propel with random trajectories at an average speed, $V \sim 35\text{-}40 \mu\text{m s}^{-1}$. The swimming characteristics is strongly determined by the Péclet number $Pe = \frac{aV}{D}$ associated with their motion. Here, a is the droplet size, V is the experimentally measured time-averaged droplet speed, and D is the diffusivity of micelles/surfactants. Following the protocol outlined by Hokmabad *et al.* [30], the diffusivity D of filled micelles is calculated to be $\sim 25 \mu\text{m}^2\text{s}^{-1}$, resulting in $Pe \sim 75$, and the droplet being a weak pusher.

Addition of PEO as a macromolecular solute results in lower droplet speed, $\sim 1\text{-}3 \mu\text{m s}^{-1}$, with more persistent trajectories. The rate of droplet solubilization remains unchanged, however, a disparity in length scales between the size of filled micelle and the characteristic polymer length results in the breakdown of continuum hypothesis-based prediction of diffusivity [18]. As the characteristic polymer length scale greatly surpasses the size of diffusing micelles, micelle diffusivity, D , remains almost identical to that observed in PEO-free aqueous TTAB solution. Moreover, the increase in bulk viscosity (10 Pa.s) hinders fluid convection, thereby leading to a reduction in Pe to ~ 3 . As a consequence of such low Pe , a puller swimming mode with more persistent motion is observed in the presence of a macromolecular solute (PEO). The fluid streamlines around the droplet for the case of a pusher and puller droplet are demonstrated using PIV micrographs in fig. 1(c) and (d), respectively.

B. Interactions at low Pe

Having benchmarked the experimental setup, we first focus on the pair-wise interactions between similar-sized ($\sim 50 \mu\text{m}$) active droplets in PEO+TTAB aqueous solution, corresponding to the case of low Pe regime. To avoid multi-body (three or more) interactions, low number density of 5CB droplets is maintained. Through a series of careful experiments, we capture ~ 40 pair interactions. In each of these cases, whenever a pair of droplets approached each other, they were found to scatter away after reaching a minimum distance (d_{min}). Fig. 1(e-k) illustrate a few representative trajectories of such pair interactions, exhibiting some intriguing preliminary observations. In certain cases (fig. 1(e,f)), a pair of droplets

approach each other symmetrically before parting away along mirrored trajectories. Further, despite variations in their approach angle, the divergence angle between the droplets appears to be constant. In other instances, a different behavior was observed (fig. 1(g)), characterized by the droplets diverging in nearly opposite directions in almost anti-mirrored trajectories. The key factor determining the fate of the trajectories is the time-lag in the approach of droplets. For instance, fig. 1(f) illustrates a scenario with little to no lag between the droplets as they approach each other, whereas, in fig. 1(g), a more pronounced time-lag exists. With increasing time-lag, the droplets deflect with a further loss of symmetry between their trajectories, as depicted in fig. 1(h,i). These findings highlight the critical role of time-lag in their interactions. To quantify time-lag, we determine the *overlap percentage*, defined as $\psi = \frac{(r_1+r_2)-L}{(r_1+r_2)} \times 100$. This metric estimates the maximum percentage of overlap between the 2D projected areas of the droplets, had they continued on their initial paths without any deflection. Here, r_1 and r_2 are the radii of the interacting droplets, and L is the distance between their centers at the extrapolated point of maximum overlap, as shown in the schematic in fig. 1(l). For droplets with no time-lag, the anticipated value of $\psi = 100\%$. As time-lag increases, ψ decreases and reaches 0%, wherein droplets barely make contact and deflect. Cases with $\psi < 0$, indicative of interactions wherein droplets do not overlap at all, are also assigned as $\psi = 0\%$.

After assessing the ψ values for all observed droplet interactions, we observed that instances where $\psi > 50\%$ (refer to fig. 2(a)) correspond to pair interactions where a droplet's deflection closely mirrors its partner's deflection. This reflection appears to occur about a plane passing through midpoint of their center-to-center line, as depicted in the trajectories shown in fig. 2(b). Moving forward, we turn our attention to droplet interactions with $\psi < 50\%$. In fig. 2(a), the ψ values for the 18 such pair interactions are presented, and fig. 2(c) exhibits a few representative trajectories. Interestingly, several pairs show a ψ value of 0%, suggesting that, even without any potential overlap between the droplets, they still interact. However, it is crucial to note that $\psi = 0\%$ is also applicable to situations where droplets are either entirely non-interacting, or where one droplet interacts with the trail/wake of the other droplet, which we will discuss in later sections (refer to fig. 5(e,f)). Indeed, for all such droplet-wake interactions, ψ fails to accurately represent the actual lag between the droplets. For now, our focus is limited to droplet-droplet interactions where $\psi = 0\%$, and all instances of droplet-wake interactions will be discussed later.

Numerous previous studies have highlighted the significant impact of the intricate interplay between flow field (hydrodynamics) and the concentration field (chemical

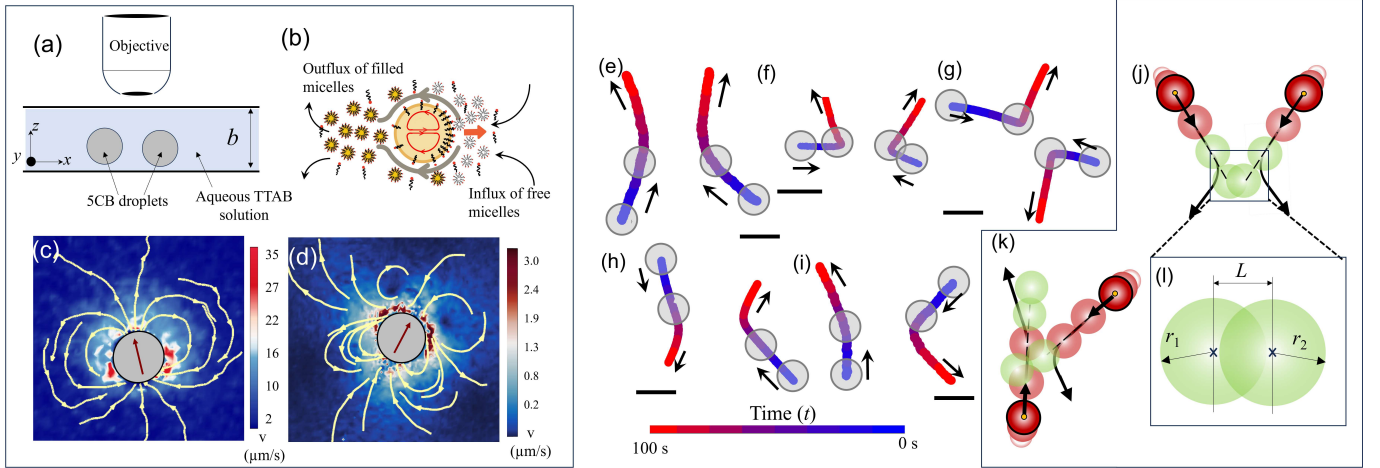


FIG. 1. (a) Schematic illustrating the experimental setup. (b) Schematic illustrating the influx/consumption of surfactant micelles and the generation of filled micelles by an active droplet during self-propelled motion. Flow-field generated by the self-propelling droplet (c) in aqueous TTAB solution where the droplet is a weak pusher and (d) in aqueous TTAB solution doped with 8000 *kDa* PEO ($c_{PEO} = 1$ wt%) where the droplet is a puller. Color bar indicates the magnitude of velocity field around the droplet. (e-i) Representative trajectories of active droplets involved in binary interactions in 1 wt.% PEO (Polyethylene oxide 8000 *kDa* molecular weight) aqueous 6 wt.% TTAB surfactant solution. Schematic showing the 2-D projected areas of approaching active droplets with no deflections. (j) case of high overlapping (k) case of no overlapping. (l) Schematic representing r_1 and r_2 as droplet radii and L as distance between the droplet centers. Scale bars indicate a length of 50 μm .

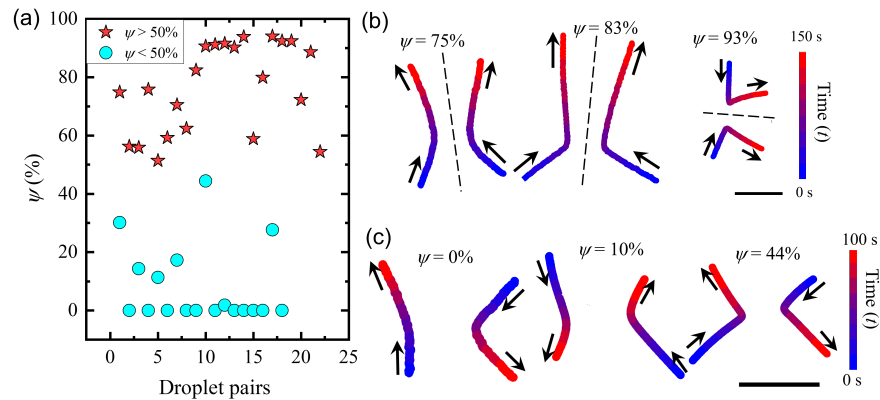


FIG. 2. (a) Overlap percentage (ψ) values for droplet pair interactions for the cases of $\psi > 50\%$ and $\psi < 50\%$. Representative trajectories of droplet pair interactions for the case of (b) $\psi > 50\%$, dotted lines represent anticipated plane of reflection and (c) $\psi < 50\%$. Scale bars indicate a length of 100 μm .

field) of solutes, such as filled micelles, on the dynamics of chemically active droplets [12, 15, 18, 23]. Consequently, we anticipate that these factors will play a crucial role in shaping the pairwise interaction of active droplets in our experiments. In the presence of PEO, since the droplets exhibit a puller swimming mode, they pull the bulk fluid in from their poles and push it out from their equatorial region. Given this hydrodynamic signature of puller droplets, we expect them to mutually attract, especially in head-on encounters. In fact, using the squirmer model, Ishikawa *et al.* predicted a hydrodynamic attraction among puller swimmers, leading

to brief period of sustained contact before they separate again [35]. Further theoretical work suggests that hydrodynamic interactions among squirmers in puller mode could lead to clustering [36–38]. Therefore, it must be noted that our findings of droplets repelling each other, regardless of their approach angle, significantly deviate from the anticipated behavior expected solely from pure hydrodynamic interaction.

In 2020, Lippera *et al.* conducted a numerical investigation of head-on pair collisions of chemically active droplets [39]. The study predicted that irrespective of the underlying Pe , the approaching droplets would con-

sistently undergo a chemical repulsion due to the accumulation of the solute in their intermediate region. Subsequently, their numerical study specifically investigated the rebounding interactions of droplet pairs, focusing on the influence of the chemical field [33]. Our experimental observations (for all ψ) are in very good agreement with these numerical predictions, reinforcing the predominance of chemical field in the observed pair-interactions.

To gain better insights into how the self-generated chemical field affects the interaction between a pair of droplets, we analyzed the chemical field distribution surrounding an isolated active droplet. This was accomplished by infusing the droplet with oil-soluble dye Nile Red. Since the droplet self-propulsion is accompanied by a continuous release of filled micelles through micellar solubilization, doping the droplet with dye enables visualization and estimation of the chemical field of filled micelles around the droplet [18, 21, 30]. Using fluorescence microscopy, with a laser at a wavelength of 560 nm, allowed us to both visualize and measure the fluorescent intensity $I(r, \alpha)$, extending radially from the droplet surface at various angles α , measured with respect to the direction of propulsion, as depicted in the inset of fig. 3(a). Using the highest (I_{max}) and lowest (I_{min}) value of intensity $I(r, \alpha)$, we computed $I^* = \frac{I(r, \alpha) - I_{min}}{I_{max} - I_{min}}$, which, as illustrated in fig. 3(b), demonstrates a monotonic decay with radial distance (r) for an active droplet at different angular positions (α). In the front region of the droplet (such as $\alpha = 0^\circ, 30^\circ, 60^\circ$, and 90°), the decay length ($\lambda(\alpha)$) of I^* , ranges from $\sim 25 \mu\text{m}$ to $35 \mu\text{m}$. Whereas, in the rear region (at angles beyond 90° , such as $120^\circ, 150^\circ$, and 180°), I^* does not decay completely, indicating an extended presence of filled micelles. The asymmetric distribution of filled micelles is expected due to the advection-driven transport of filled micelles towards the rear end of the droplet, forming an extended trail (see fig. 3(a)). However, it is to be noted that the concentration field in the anterior region for a droplet in PEO + TTAB aqueous solution is significantly higher compared to that for a droplet in PEO-free aqueous TTAB solution (see fig. 3(c,d)). In the presence of PEO, droplets swim with a lower Pe , wherein the relatively weaker advection of the surrounding fluid is unable to sweep away the filled micelles towards the rear of the droplet, with as much strength as droplets swimming at relatively higher Pe in PEO-free aqueous TTAB solution. Hence, in PEO solution, whenever two droplets approach in any orientation, the accumulation of filled micelles in the intermediate region significantly hampers the supply of fresh surfactants [40]. Consequently, in line with the negative chemotactic behavior [21], the droplets alter their paths in search of fresh fuel, thus moving apart, and thereby reinstating the necessary interfacial polarity for their motion.

With this understanding of the distribution of the chemical field surrounding the droplets, we now discuss the differences in the pair-wise interactions observed at

higher and lower ψ values. Illustrated in fig. 3(e) is a schematic representative of the closest approach (at d_{min} .) of a pair of droplets with $\psi > 50\%$. Due to the accumulation of filled micelles, the droplets are prevented from direct contact; the overlap of their chemical plumes generates chemo-repulsive interactions. Following their interaction, it is anticipated that the droplets will move towards regions not already occupied by filled micelles, thereby re-establishing a supply of fresh surfactants. If we identify the yellow droplet on the left as the probe droplet, it can then move away from filled micelle zones, to either region *I* or *II*. Given that both the droplets are identical and their approach is symmetric, their responses are also expected to be symmetric. Should the probe droplet head towards region *I*, its counterpart is expected to proceed to region *II*. This, however, would lead to overlapping paths, which is prohibited. Consequently, the probe droplet is compelled to move exclusively towards region *II*, with its partner heading to region *I*, thus creating trajectories that are reflective of one another. Similarly, fig. 3(f) displays a schematic representation of the droplets at d_{min} . with a lesser potential overlap (i.e. ψ below 50%). Considering the filled micelles in regions *I* and *III*, the probe droplet has the option to advance towards region *IV* or *II*. Should the droplet head toward region *II*, leading the partner droplet to choose region *IV*, their paths would intersect, which is to be avoided. Hence, the droplets are likely to move towards regions *IV* and *II*, respectively, resulting in paths that do not mirror each other. As depicted in the schematics, we determined the incoming angle (θ_{in}), formed between the droplet velocity vector and the line joining the centers of the two droplets at d_{min} , for all pair-interactions. As discussed earlier, for all droplet-droplet interactions, we will limit our focus on interactions where $\theta_{in} \leq 90^\circ$ for both droplets at their minimum separation, d_{min} . Further, $\delta\theta$ measures the change in orientation of a droplet's velocity vector before and after the interaction. Fig. 3(g) illustrates the variation in $|\delta\theta|$ with respect to the $|\theta_{in}|$, for all observed pair encounters. Notably, regardless of whether ψ is above 50% or below 50%, $|\delta\theta|$ shows an inverse correlation with $|\theta_{in}|$. This leads to $\beta \equiv |\theta_{in}| + |\delta\theta|$ being nearly constant, irrespective of changes in $|\theta_{in}|$, as depicted in fig. 3(h). Here, β represents the angle between the velocity vector of droplet after deflection and the center-to-center line (fig. 4(a)), and its range falls within 90° to 120° .

We now return to the measurement of radial decay of I^* for different angular position (α) around an active droplet (fig. 3(b)), which demonstrates that the decay length of I^* remains nearly the same at its front ($\alpha = 0^\circ$ to $\alpha = 90^\circ$). As a result, the accumulation of filled micelles at the front of the droplet assumes a nearly circular form. Hence, when the plumes of the droplets touch each other, with both $|\theta_{in}| < 90^\circ$, at their nearest point of approach, the contact point is located along the line

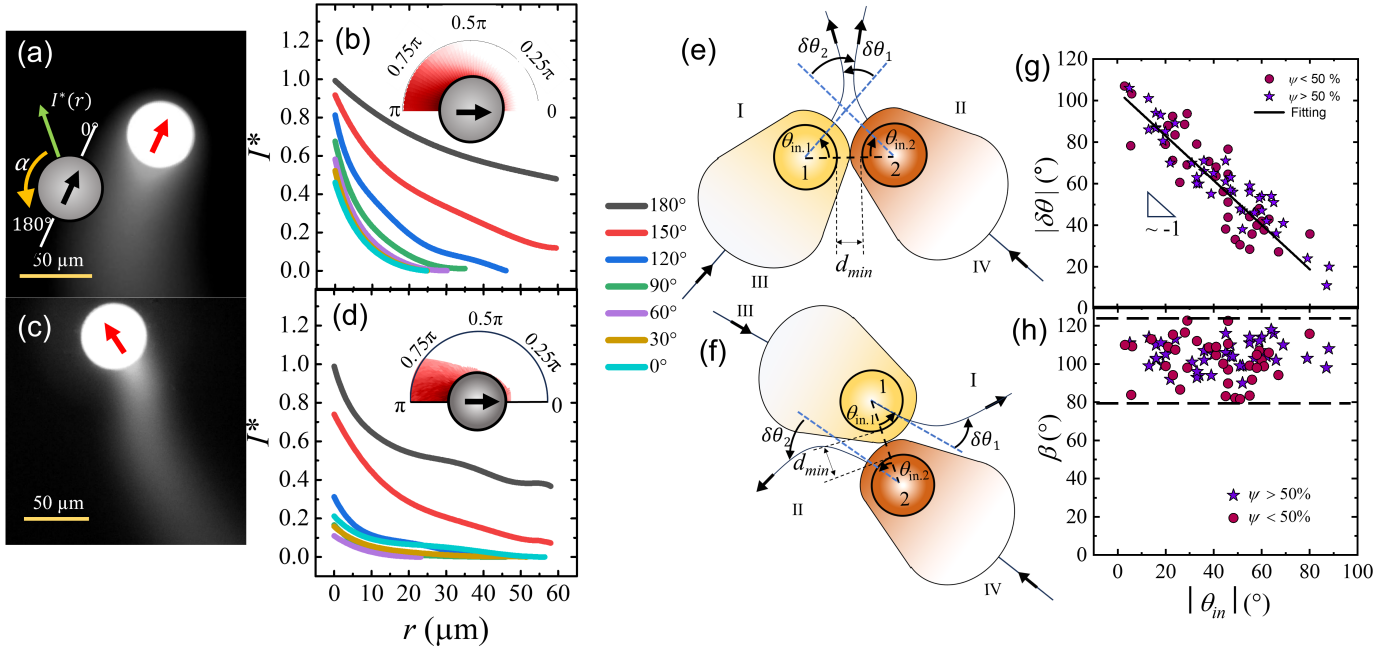


FIG. 3. Fluorescence micrograph (greyscale) of an active 5CB droplet in aqueous 6 wt.% TTAB surfactant solution (a) with 1 wt.% PEO (Polyethylene oxide 8000 kDa molecular weight) (c) with just water. The inset displays a schematic illustrating the measurement of fluorescent intensity (I^*) in the radial direction (r) at angular coordinates ranging from 0° to 180° . Radial variation in fluorescence intensity I^* around an active droplet starting from the droplet surface, at different angular positions (b) in 1 wt.% PEO and (d) in just water. Schematic illustrating collision of the plume of filled micelles in droplet-droplet interaction for the case of (e) $\psi > 50\%$ and (f) $\psi < 50\%$. Red colored plume around droplet schematic represents the value of I^* ranging from 0 to 1. The yellow-colored droplet in (e) and (f) serves as the probe droplet, forming the basis of the discussion. Schematic also illustrates the approaching angle (θ_{in}), change in droplet orientation ($\delta\theta$), and minimum surface-to-surface distance between interacting droplets (d_{min}) for the two cases. (g) Variation in $|\delta\theta|$ with respect to $|\theta_{in}|$. (h) Variation in β with respect to $|\theta_{in}|$.

connecting their centers. Additionally, $|\theta_{in}|$ and β denote the angles between the incoming and outgoing velocity vectors relative to the impact point, respectively (see fig. 4(a)). To understand the invariance of β with respect to $|\theta_{in}|$, we plot I^* as well as $\frac{dI^*}{d\alpha}$ as a function of angular position α near the interface of an isolated moving droplet (see fig. 4(b)). The plot reveals a monotonic increase in I^* from the front (0°) to the rear of the droplet (180°), consistent with the higher concentration of filled micelles in the droplet's wake than in its front. For α less than 90° , I^* increases gradually. However, between 90° and 120° , I^* rises sharply, indicating a rapid accumulation of filled micelles in this region. Beyond 120 - 130° , rate of increase in I^* again falls, and it eventually plateaus about 180° . This distribution suggests the existence of a transition zone between 90° and 120° , marking a sudden shift from lower to higher concentrations of filled micelles near the droplet's surface. This polar asymmetry in the filled micelle concentration, combined with axisymmetric propulsion, ensures sustained propulsion of an isolated droplet in the same direction, until influenced by external concentration fluctuations.

During a pair interaction, when the plumes of the filled micelles touch each other, the inherent angular asymmetry of the filled micelle concentration is disrupted at the impact point and an axial asymmetry is also introduced, as illustrated in schematic shown in fig. 4(a). Although Pe is low, the diffusion timescale needed for the micelles to disperse and reinstate the droplets' natural chemical polarity ($\tau_{diffuse} = \frac{R^2}{D} \sim 100$ s) is longer than the timescale of droplet motion ($\tau_{translation} = \frac{R}{V} \sim 25$ s). This necessitates a change in the propulsion direction, re-aligning the droplet by an angle $\sim 90^\circ$ to 120° with respect to the contact point, which effectively re-establishes the original asymmetry in their chemical field. The magnitude of this deflection depends upon the severity of the penalty in chemical asymmetry enforced during the interaction. Therefore, lower values of θ_{in} result in higher $\delta\theta$, and vice-versa. Hence, irrespective of θ_{in} , β consistently approximates values within the range of 90° to 120° . For the case of droplets interacting with high overlap ($\psi > 50\%$) and mirrored trajectory, this manifests in droplets diverging at same angle independent of their approach orientations. In 2020, Lippera *et al.*

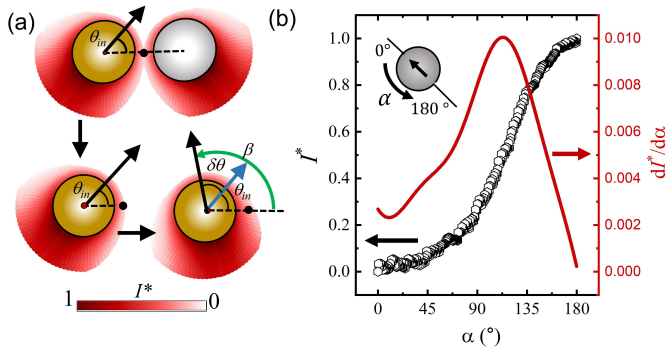


FIG. 4. (a) Schematic depicting the impact point where filled micelles from interacting droplets meet. Further the change in the droplet direction in the event of encounter of filled micelles from the partner droplet at impact point. Black and blue arrows represent the direction of droplet movement before and after deflection, respectively. Red colored plume around droplet schematic represents the value of I^* ranging from 0 to 1. (b) Variation in I^* and $\frac{dI^*}{d\alpha}$ with respect to α along the droplet interface in the case PEO+TTAB solution.

forecasted that regardless of the initial approach angle, droplets alter their swimming direction such that their departing velocity vectors form an angle that is nearly constant $\sim 60^\circ$ (equivalent to $\beta \sim 120^\circ$) [33]. Our experimental observations showcase a striking correspondence with the predictions made by Lippera *et al.*, thereby reinforcing the validity of their model. Further, our study demonstrates that this observation remains true, even for the case of non-symmetric collisions (i.e., for $\psi < 50\%$).

Fig. 5(a) demonstrates the evolution of droplet speed, V , during pair-wise interaction for different values of θ_{in} . It is evident that a droplet with lower values of θ_{in} experiences a greater relative magnitude of change in speed, leading to a higher overall change in momentum. This momentum change stems from the chemo-repulsive interaction due to the build-up of filled micelles between the surfaces of the droplets. With a reduction in the gap between the droplet surfaces, the micellar accumulation builds up, resulting in a higher repulsion. Consequently, for lower values of θ_{in} , wherein the droplets have to undergo maximum deflection, they approach closer (i.e., attain a lower d_{min}), and experience stronger repulsion. This is supported by an increasing trend in d_{min} with respect to $\theta_{in,avg} = \frac{\theta_{in,1} + \theta_{in,2}}{2}$, where $\theta_{in,1}$ and $\theta_{in,2}$ are the incident angles of the two interacting droplets, shown in fig. 5(b). Fig. 5(c) reveals that the duration (Δt) over which the translational velocity V deviates from its initial pre-collision value, exceeds the Δt during which the rate of change in angular speed ($|\frac{d\theta}{dt}|$) is nonzero. This difference, denoted as Δt_{diff} , suggests that even after the cessation of droplet rotation, the sustained accumulation of the chemical field maintains an elevated translational

movement of the rebounding droplets. This argument is supported by the decreasing behavior of Δt_{diff} with respect to θ_{in} , as shown in fig. 5(d). For lower θ_{in} , due to higher velocity component along the droplet center-to-center line, the higher overlap of the chemical fields prolongs the effect on translation motion, i.e., higher Δt_{diff} . On the other hand, since the extent of overlap of plumes is lesser in cases with higher θ_{in} , the effect wanes off with smaller Δt_{diff} .

Next we discuss the interaction of droplets with the chemical trails left by other droplets for which $\theta_{in} > 90^\circ$. Fig. 5(e) depict representative trajectories of such interactions. Fig. 5(f) presents the variation of β ($= \theta_{in} + \delta\theta$), as described in the schematic shown in the inset, with varying incident angle θ_{in} . Similar to our observations for droplet-droplet interactions, we observe that regardless of their initial approach direction, droplets consistently rebound with β values ranging between 90° and 120° . This observation further underscores the conclusion that the rebounding behavior of the droplet is mainly decided by the self-generated chemical polarity of the droplets.

C. Interactions at higher Pe

The observations in the previous section emphasize the significance of chemical field-driven repulsive interactions between droplet-droplet/wake at low Péclet numbers (Pe). To contrast these findings with pair-wise interactions at relatively higher Pe values, where the hydrodynamic effects are expected to guide the droplet interactions, we explore interactions of 5CB droplets in PEO-free aqueous TTAB solution, wherein $Pe \sim 75$. We observed ~ 20 pair interactions, and a few of the representative trajectories are shown in fig. 6(a-c). In contrast to the behavior observed at lower Pe values, it is observed that droplets approach very close, occasionally even making sustained contact. On approaching from the same direction, they typically move in unison for sometime before separating. This synchronous motion can occur with multiple formations, such as (a) side-by-side (fig. 6(a)), where droplets stay close at each others equatorial positions, a configuration typical when θ_{in} is less than or equal to 90° ; and (b) staggered (fig. 6(b)), where one droplet trails the other at an angle, commonly observed when a droplet's θ_{in} is between 90 and less than 180° . These configurations often shift from side-by-side to staggered before the droplets part ways. Further, when droplets meet head-on from opposite directions with low θ_{in} , they almost make contact, pause briefly, and then move apart, as illustrated in fig. 6(c).

Unlike low Pe systems, the absence of strong repulsive interaction indicates relatively inferior chemical interactions. Better understanding of these observations is extracted by investigating the angular variation of

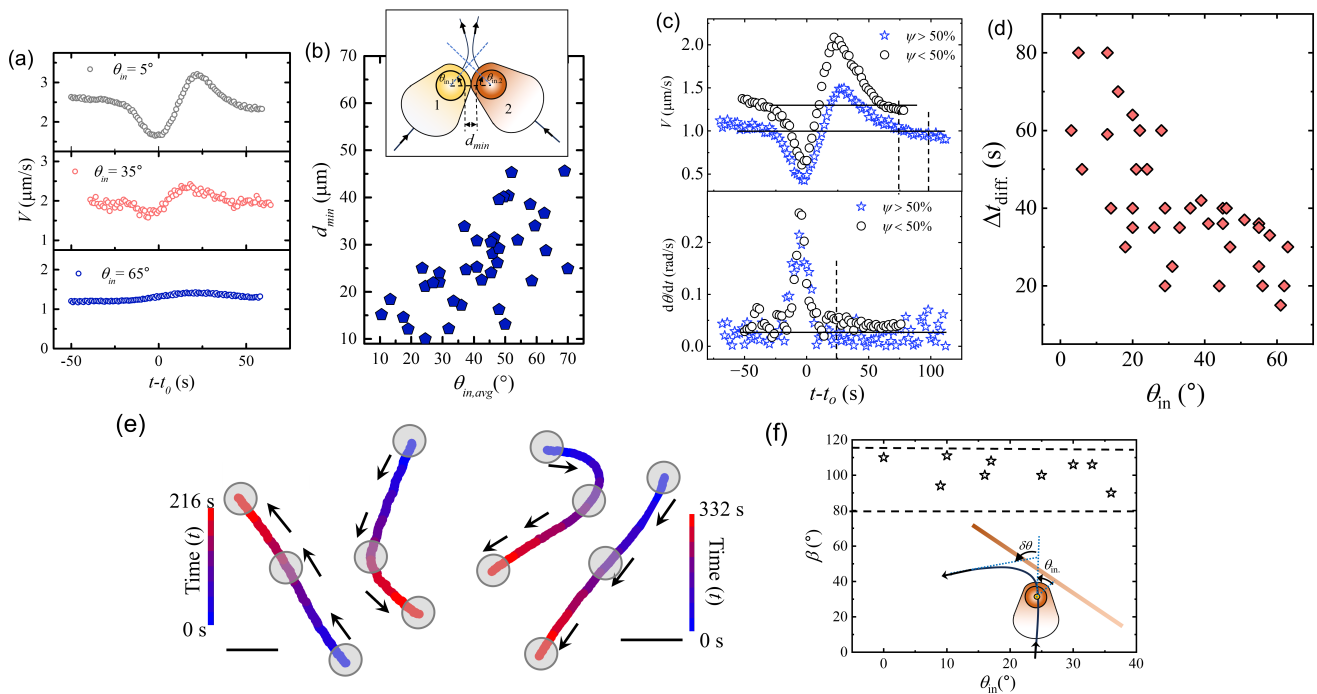


FIG. 5. (a) Evolution in droplet speed V during pairwise interaction for different cases of θ_{in} . The t_0 is the reference time representing the moment when the distance between the surfaces of the droplets reaches d_{min} . (b) Variation in d_{min} with respect to $\theta_{in,avg}$. Schematic in the inset illustrates d_{min} . (c) Evolution in droplet speed V and the rate of change in droplet orientation ($|\frac{d\theta}{dt}|$) during pairwise interaction in case of $\psi > 50\%$ and $\psi < 50\%$. (d) Variation in Δt_{diff} with respect to the θ_{in} . (e) Representative trajectories of droplet interaction with trail/wake of other droplet in case of aqueous 1 wt.% PEO solution. Scale bars indicate a length of $100 \mu\text{m}$. (f) Variation in β with respect to the $\theta_{in, trail}$ in droplet-trail interactions. Inset to the figure illustrates the definition of angles.

the chemical field around an isolated droplet navigating through an aqueous TTAB solution, as reflected by the normalized fluorescence intensity I^* (refer to fig. 3(c,d)). In the anterior region of the droplet (i.e., at angles of 0° , 30° , 60° , and 90°), I^* is remarkably lower compared to the case of droplet at low Pe . However, in the rear region (beyond 120°), the intensity values increase sharply, implying that the presence of filled micelles is confined to a narrow wake region of the active droplet, while being almost absent at its front and sides. Notably, the intensity levels at angles of 150° and 180° are actually lower at higher Pe values, than those observed in lower Pe settings. This difference is attributed to the stronger advection at higher Pe , which effectively convects away the filled micelles to the droplet's rear, thereby diminishing their overall concentration. This reduction in the concentration of filled micelles leads to a decreased chemotactic repulsion among the droplets. As such, the observation of attraction, albeit weak, is an evidence of significant influence of hydrodynamics in the pair-interactions as seen in fig. 6 (a-c). At $Pe \sim 75$, these droplets are known to swim with weak pushing gait, which was confirmed through PIV experiments (see fig. 1(c)). In 2010, Götze *et al.* theoretically demonstrated a pair of strong pusher

squirmers to indefinitely maintain a side-by-side configuration [41]. However, introducing orientational fluctuations was found to induce separation. Our findings confirm the predictions made by Götze *et al.*, highlighting the significance of droplet hydrodynamics in their pairwise interactions at higher Pe . Further, the local time-dependent fluctuations in surfactant concentration at the interface introduce the orientation fluctuations in droplet motion [17] which result in their eventual separation. During their head-on approach, the absence of strong chemotactic repulsion facilitates very low d_{min} . This is despite the outwardly emanating streamlines from the front of the droplets, which theoretically ought to hydrodynamically repel the droplets. However, it is only once they approach very close that the short range ($\sim \frac{1}{\gamma\beta}$) hydrodynamic interaction results in their separation. Overall, our observations are in line with prior theoretical investigations that suggested that the pusher squirmer would move together due to the hydrodynamic attraction [41–44]. They also align with recent experimental evidence from studies on micellar solubilization-based active droplets in surfactant solutions, where hydrodynamic interactions have been observed to result in the formation of metastable lines [45] and clustering [29].

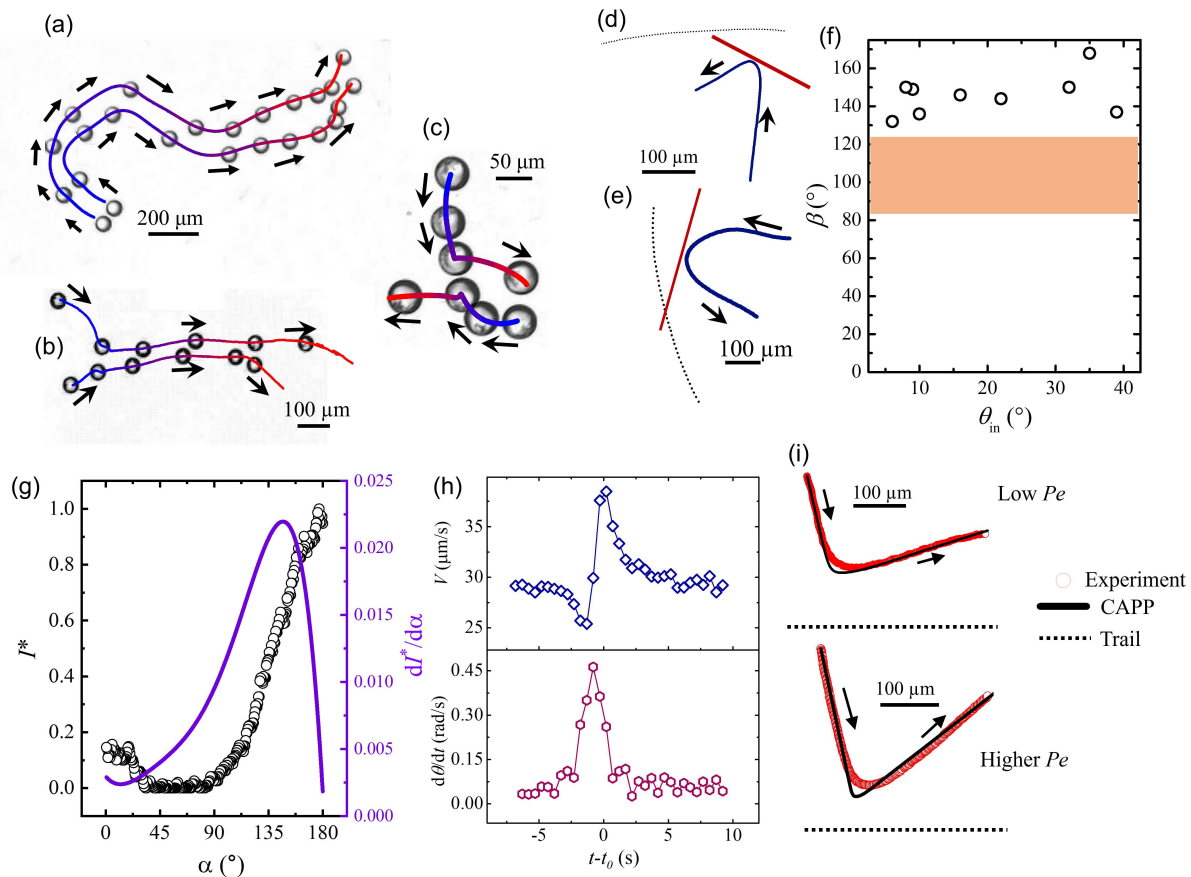


FIG. 6. For active 5CB droplets swimming in aqueous 6 wt.% TTAB surfactant solution (a-c) Representative trajectories of pairwise interactions. (d,e) Representative trajectories of droplets interacting with chemical trails left behind by other swimming droplets. Dotted black line represents the center line of the chemical trail and solid red line is the anticipated reflective line. (f) Variation of β with incident angle $\theta_{in, trail}$ in case of water. Inset to the figure illustrates the definition of angles. (g) Variation in I^* and $\frac{dI^*}{d\alpha}$ with respect to the α along the droplet interface in case of water. (h) Representative variation of V and $|\frac{d\theta}{dt}|$ with time in case of water. t_0 represents the reference time at which the distance between the droplet and the center line along the trail is minimum. (i) Representative trajectories showing the droplets rebounding during the interaction with the trail/wake of other droplet. Black dotted lines represents the orientation of the trail left behind by other swimming droplets. Overlaid black line on droplet trajectories represents the trajectories obtained using CAPP model.

Fig. 6(d-e) depict representative trajectories of droplet-wake interactions at high Pe , with dotted lines indicating the wake of a droplet, and solid blue lines representing the interacting droplet trajectories. Fig. 6(f) presents the variation of β ($= \theta_{in} + \delta\theta$), with varying incident angle θ_{in} , for a few such interactions. Similar to our observations at low Péclet numbers (Pe), we observed that regardless of their initial approach direction, droplets consistently rebound with β values ranging between 130° and 150° . It is noteworthy to emphasize that the range of β values for aqueous TTAB solution (shown by markers) exceeds that of TTAB+PEO aqueous solution (shaded region in fig. 6(f)). This observation aligns with the chemical rebounding phenomenon, which is influenced by the inherent chemical polarity of the droplets. This difference in interfacial chemical polarity for 5CB

droplets swimming in low vs high Pe systems is indicated by the angular variation of I^* shown in fig. 4(b) and fig. 6(g). For aqueous TTAB solution, Hokamabad *et al.* [30], reported that active droplets “reflect” when interacting with the chemical wake of other droplets. Numerical analysis using the chemically active polar particle (CAPP) approach was further illustrated to match with the experimental findings. While these computational analyses agree with seemingly reflective trajectories, they do not account for the droplet’s inherent Pe -dependent chemical polarity. Fig. 6(d-e) highlights that the expected reflection planes (solid red lines) do not coincide with the droplet wake (dotted black lines). This discrepancy emphatically indicates that the droplets’ behavior can be more complex than mere reflection about the wake. Unlike low Pe case, for these interactions, both

angular speed ($|\frac{d\theta}{dt}|$) and translation speed, V , return to their pre-collision value at around same time, i.e., $\Delta t_{\text{diff}} \sim 0$, see fig. 6(h). This is again attributed to the relatively weaker strength of chemical interactions at higher Pe .

TABLE I. Comparison of dimension-less coupling constants obtained for fitting the X-Y trajectories using the CAPP model.

Pe	$\frac{\Omega c_0}{vR}$	$\frac{\alpha c_0}{vR^2}$
Low (TTAB+PEO solution)	12	12.8
High (TTAB solution)	60	8

Finally, we use the CAPP model [46] to predict the droplet-wake interaction for the case of both low and high Pe . The wake is assumed to be a quasi-static 1D diffusing concentration field in the y -direction, with the source located at $y = 0$. The evolution of the droplet position and its orientation as it interacts with the wake is obtained from the Langevin dynamics (ignoring random fluctuations) as

$$\dot{x} = V \cos \theta, \quad (1a)$$

$$\dot{y} = V \sin \theta + \frac{\alpha c_0 y}{\sqrt{2\pi} (2D\Delta t)^{3/2}} \exp\left(-\frac{y^2}{4D\Delta t}\right), \quad (1b)$$

$$\dot{\theta} = \frac{\Omega c_0 y}{\sqrt{2\pi} (2D\Delta t)^{3/2}} \exp\left(-\frac{y^2}{4D\Delta t}\right) \cos \theta. \quad (1c)$$

The model has two fitting parameters, Ωc_0 and αc_0 , which represent the strength of effective torque and the effective translational deceleration experienced by the droplet, respectively. To ensure a valid comparison between the low and high Pe cases, we normalize the coupling constants with respect to VR and VR^2 , respectively. The normalized coupling constants are listed in Table I. The values indicate that at higher Pe , droplets experience a higher torque ~ 5 times than at lower Pe , which is consistent with the higher β values observed for droplets at higher Pe in order to re-establish their inherent chemical polarity. Further, droplets at lower Pe experience a more pronounced translational deceleration/acceleration, consistent with increased accumulation of filled micelles in intermediate region, leading to chemo-repulsive interactions. The predicted and experimental droplet trajectories for high and low Pe droplet-wake interactions are depicted in fig. 6(i), and are found to be in good agreement.

IV. CONCLUSIONS

This study presents a comprehensive investigation into the pair-wise interactions of chemically active droplets swimming at different Péclet numbers (Pe). At low Pe values, the observed pair-wise interactions between approaching droplets showcases a distinctive scattering behaviour, wherein, after reaching a minimum distance the droplets rebound without engaging in direct physical contact. This rebounding/scattering phenomenon is attributed to the dominant influence of the accumulation of chemical field emanating from the filled micelles. Due to the low advective effects, in comparison to the diffusive effects of filled micelles, the influence of the hydrodynamic field is minimal at low Pe , thereby allowing chemo-repulsive interactions to outweigh the contribution from their hydrodynamic interactions. The findings of this study provide excellent experimental evidence supporting the conclusions drawn from the theoretical studies by Michelin and co-workers [33, 39]. In contrast to low Pe conditions, droplets swimming at higher Pe demonstrate dominance of hydrodynamic fields in their pair-wise interactions thus allowing droplets to attract and even sustain contact. Our study also demonstrates that, independent of the underlying Pe , in both cases, droplet-wake interactions are influenced primarily by the repulsive chemical interactions. The chemical rebounding is always decided by the inherent chemical polarity of the deflecting droplet which is determined by its Pe . This study provides compelling evidence highlighting the significant influence of both hydrodynamic and chemical fields on the dynamics of active droplets during their pair-wise interactions across a wide range of Péclet numbers (Pe). The observed results offer valuable insights that contribute to a deeper understanding of multibody interactions within active droplet systems. Moreover, the implications of this research extend to the potential for controlling and manipulating such interactions under diverse Pe conditions.

ACKNOWLEDGEMENT

We acknowledge the funding received from the Science and Engineering Research Board (ECR/2018/000401 and CRG/2022/003763), and from Department of Science and Technology, India (SR/FST/ETII-055/2013).

[1] J. L. Anderson, Annual review of fluid mechanics **21**, 61 (1989).

[2] J. R. Howse, R. A. Jones, A. J. Ryan, T. Gough, R. Vafabakhsh, and R. Golestanian, Physical review letters **99**, 048102 (2007).

- [3] R. Golestanian, T. B. Liverpool, and A. Ajdari, *Physical review letters* **94**, 220801 (2005).
- [4] H.-R. Jiang, N. Yoshinaga, and M. Sano, *Physical review letters* **105**, 268302 (2010).
- [5] J. Palacci, S. Sacanna, A. P. Steinberg, D. J. Pine, and P. M. Chaikin, *Science* **339**, 936 (2013).
- [6] W. F. Paxton, K. C. Kistler, C. C. Olmeda, A. Sen, S. K. St. Angelo, Y. Cao, T. E. Mallouk, P. E. Lammert, and V. H. Crespi, *Journal of the American Chemical Society* **126**, 13424 (2004).
- [7] A. M. Brooks, M. Tasinkevych, S. Sabrina, D. Velegol, A. Sen, and K. J. Bishop, *Nature communications* **10**, 495 (2019).
- [8] P. Dwivedi, D. Pillai, and R. Mangal, *Current Opinion in Colloid & Interface Science*, 101614 (2022).
- [9] K. Peddireddy, P. Kumar, S. Thutupalli, S. Herminghaus, and C. Bahr, *Langmuir* **28**, 12426 (2012).
- [10] S. Michelin, *Annual Review of Fluid Mechanics* **55**, 77 (2023).
- [11] S. Birrer, S. I. Cheon, and L. D. Zarzar, *Current Opinion in Colloid & Interface Science* **61**, 101623 (2022).
- [12] M. Morozov and S. Michelin, *The Journal of chemical physics* **150**, 044110 (2019).
- [13] A. Izzet, P. G. Moerman, P. Gross, J. Groenewold, A. D. Hollingsworth, J. Bibette, and J. Brujic, *Physical Review X* **10**, 021035 (2020).
- [14] P. Dwivedi, B. R. Si, D. Pillai, and R. Mangal, *Physics of Fluids* **33** (2021).
- [15] B. V. Hokmabad, R. Dey, M. Jalaal, D. Mohanty, M. Al-mukambetova, K. A. Baldwin, D. Lohse, and C. C. Maass, *Physical review X* **11**, 011043 (2021).
- [16] M. Suga, S. Suda, M. Ichikawa, and Y. Kimura, *Physical Review E* **97**, 062703 (2018).
- [17] S. Suda, T. Suda, T. Ohmura, and M. Ichikawa, *Physical Review Letters* **127**, 088005 (2021).
- [18] P. Dwivedi, A. Shrivastava, D. Pillai, and R. Mangal, *Soft Matter* **19**, 4099 (2023).
- [19] M. Kumar, A. Murali, A. G. Subramaniam, R. Singh, and S. Thutupalli, *arXiv preprint arXiv:2303.10742* (2023).
- [20] P. Dwivedi, A. Shrivastava, D. Pillai, N. Tiwari, and R. Mangal, *Soft Matter* (2023).
- [21] C. Jin, C. Krüger, and C. C. Maass, *Proceedings of the National Academy of Sciences* **114**, 5089 (2017).
- [22] R. Dey, C. M. Bunes, B. V. Hokmabad, C. Jin, and C. C. Maass, *Nature communications* **13**, 1 (2022).
- [23] P. Dwivedi, A. Shrivastava, D. Pillai, and R. Mangal, *Physics of Fluids* **33**, 082108 (2021).
- [24] A. C. Castonguay, R. Kailasham, C. M. Wentworth, C. H. Meredith, A. S. Khair, and L. D. Zarzar, *Physical Review E* **107**, 024608 (2023).
- [25] N. Verstraeten, K. Braeken, B. Debkumari, M. Fauvart, J. Fransaer, J. Vermant, and J. Michiels, *Trends in microbiology* **16**, 496 (2008).
- [26] B.-L. Tang, J. Yang, X.-L. Chen, P. Wang, H.-L. Zhao, H.-N. Su, C.-Y. Li, Y. Yu, S. Zhong, L. Wang, *et al.*, *Nature communications* **11**, 285 (2020).
- [27] C. D. Nadell, J. B. Xavier, and K. R. Foster, *FEMS microbiology reviews* **33**, 206 (2008).
- [28] S. Thutupalli, R. Seemann, and S. Herminghaus, *New Journal of Physics* **13**, 073021 (2011).
- [29] B. V. Hokmabad, A. Nishide, P. Ramesh, C. Krüger, and C. C. Maass, *Soft matter* **18**, 2731 (2022).
- [30] B. V. Hokmabad, J. Agudo-Canalejo, S. Saha, R. Golestanian, and C. C. Maass, *Proceedings of the National Academy of Sciences* **119**, e2122269119 (2022).
- [31] C. H. Meredith, P. G. Moerman, J. Groenewold, Y.-J. Chiu, W. K. Kegel, A. van Blaaderen, and L. D. Zarzar, *Nature Chemistry* **12**, 1136 (2020).
- [32] P. T. Underhill, J. P. Hernandez-Ortiz, and M. D. Graham, *Physical review letters* **100**, 248101 (2008).
- [33] K. Lippera, M. Benzaquen, and S. Michelin, *Soft Matter* **17**, 365 (2021).
- [34] W. Thielicke and R. Sonntag, *Journal of Open Research Software* **9** (2021).
- [35] T. Ishikawa, M. Simmonds, and T. J. Pedley, *Journal of Fluid Mechanics* **568**, 119 (2006).
- [36] A. Zöttl and H. Stark, *Physical review letters* **112**, 118101 (2014).
- [37] M. Theers, E. Westphal, G. Gompper, and R. G. Winkler, *Soft Matter* **12**, 7372 (2016).
- [38] M. Theers, E. Westphal, K. Qi, R. G. Winkler, and G. Gompper, *Soft matter* **14**, 8590 (2018).
- [39] K. Lippera, M. Morozov, M. Benzaquen, and S. Michelin, *Journal of Fluid Mechanics* **886**, A17 (2020).
- [40] M. Morozov, *Soft Matter* **16**, 5624 (2020).
- [41] I. O. Götze and G. Gompper, *Physical Review E* **82**, 041921 (2010).
- [42] G. Guan, J. Lin, and D. Nie, *Entropy* **24**, 1564 (2022).
- [43] Z. Ouyang, J. Lin, and X. Ku, *International Journal of Non-Linear Mechanics* **108**, 72 (2019).
- [44] A. Kanevsky, M. J. Shelley, and A.-K. Tornberg, *Journal of Computational Physics* **229**, 958 (2010).
- [45] S. Thutupalli, D. Geyer, R. Singh, R. Adhikari, and H. A. Stone, *Proceedings of the National Academy of Sciences* **115**, 5403 (2018).
- [46] S. Saha, R. Golestanian, and S. Ramaswamy, *Physical Review E* **89**, 062316 (2014).